**Journal of the European Optical
Society-Rapid Publications**

RESEARCH ARTICLE　　　　　　　　　　　　　　　　　　　　　　　**OPEN** 🔓 **ACCESS**

Accurate calibration of optical tweezers close to a glass surface using interference rings in backscattered light

Flavie Gillant[1], Julien Moreau[1], Maximilian U. Richly[2], Antigoni Alexandrou[2], Karen Perronet[1,3],
and Nathalie Westbrook[1,*] 🔴

[1] Université Paris-Saclay, Institut d'Optique Graduate School, CNRS, Laboratoire Charles Fabry, 91127 Palaiseau, France
[2] Laboratoire d'Optique et Biosciences, Ecole Polytechnique, CNRS, INSERM, Université Paris-Saclay, 91128 Palaiseau, France
[3] Université Paris-Saclay, Ecole Normale Supérieure Paris-Saclay, CNRS, CentraleSupélec, LuMIn, 91190 Gif-sur-Yvette, France

Abstract. Mechanical forces play an important role in the behaviour of cells, from differentiation to migration and the development of diseases. Optical tweezers provide a quantitative tool to study these forces and must be combined with other tools, such as phase contrast and fluorescence microscopy. Detecting the retro-reflected trap beam is a convenient way to monitor the force applied by optical tweezers, while freeing top access to the sample. Accurate in situ calibration is required especially for single cells close to a surface where viscosity varies rapidly with height. Here, we take advantage of the well contrasted interference rings in the back focal plane of the objective to find the height of a trapped bead above a cover slip. We thus map the viscous drag dependence close to the surface and find agreement between four different measurement techniques for the trap stiffness down to 2 µm above the surface. Combining this detection scheme with phase contrast microscopy, we show that the phase ring in the back focal plane of the objective must be deported in a conjugate plane on the imaging path. This simplifies implementation of optical tweezers in combination with other techniques for biomechanical studies.

Keywords: Optical tweezers, Optical micromanipulation, Optical trapping.

1 Introduction

Optical tweezers are widely used in biophysics to study mechanical properties of single systems, from the molecular to the cellular level [1–3]. For precise force measurements, micron-sized beads are specifically linked to the biological system under study and act as well defined handles. The force applied on these beads must be calibrated before it is applied to the biological system. Many calibration techniques have been developed [4], such as power-spectrum analysis [5], drag force, escape force, equipartition [6], direct force measurement by optical momentum transfer [7, 8], step-response [9–11], Bayesian inference [12] and machine learning [13].

Most calibration techniques use forward scattering by the bead collected by a condenser and image the back-focal plane of this condenser on a quadrant photodiode or a position sensitive detector in order to be sensitive only to the displacement of the bead within the trap [7–9, 14]. However, detecting small displacements of the bead requires collecting the transmitted light over a large numerical aperture. It thus makes sense to use the same high NA objective both for trapping and detecting, and to collect back scattered instead of forward scattered light for calibration [15]. In addition, transmitted light is sometimes blocked by the sample itself for example when studying nanopores [16–18] or by the annular diaphragm in the condenser when using dark-field imaging [19]. In many respects, calibration techniques using trapping light transmitted by the bead are transposable to the reflection setups. In transmission, interference between light reflected by the bead and light reflected at the coverslip-water interface induces a small modulation of the total intensity that can be used to infer the height of the bead [20]. In reflection, this interference plays a stronger role due to its higher contrast. Some authors have used the modulation of the total reflected intensity to infer the axial displacement of the bead [7, 10] as a complementary signal to the forward scattering. When backscattering detection is used alone for calibration, the influence of interference on the signal detected by the quadrant photodiode can be more problematic. Some experiments have used spatial filtering and

---

* Corresponding author: nathalie.westbrook@institutoptique.fr

central obturation of the back focal plane of the objective to eliminate light reflected from any other surface than the bead itself [16–18]. More recently, Samadi et al. [19] calculated numerically the signal due to the interference of the light reflected by the bead and that reflected by the coverslip. Here, we monitor this very well contrasted interference pattern and use it to measure precisely the height of the bead, needed to infer the viscous drag close to the glass surface. We check that despite this interference pattern the detection response remains linear. We compare four stiffness calibration methods, namely step-response, Bayesian inference, and the well-known power-spectrum density and equipartition calibration methods. We evaluate their accuracy as a function of the height of the bead with respect to the coverslip and of the incident trapping laser power. We then show that the use of a phase contrast objective, in this configuration, prevents the calibration, unless the phase ring can be deported in the imaging path. The conclusions in the latter case are different from the one obtained with a detection in transmission [21].

2 Experimental setup

The setup (Fig. 1) is based on an inverted microscope (Nikon, Eclipse Ti-U) and an oil immersion objective (Nikon, Plan Fluor 100X, NA = 1.3 or Plan Fluor 100X, NA = 1.3, Ph3). Beads are trapped using an Ytterbium fiber laser (Keopsys, λ = 1069 nm, TEM00, linearly polarized) delivering up to 700 mW at the entrance of the objective. Two orthogonal acousto-optic deflectors (AOD) (Intra Action Corp. DTD 274HA6) control the displacement of the trap in the transverse plane. Each AOD frequency is controlled by a home-built Direct Digital Synthetizer (DDS) with a time resolution of 2 µs. In order to get a pure translation of the trap in the sample plane, the AODs are conjugated with the back-focal plane of the objective (BFP). The laser beam is expanded in order to fill the entrance pupil of the objective (Φ_{pupil} = 5.2 mm, diameter of the laser waist before the objective Φ_{laser} = 5.3 mm).

The backscattered signal is detected by a quadrant photodiode (QPD, SPOT-9DMI, OSI Optoelectronics). All four signals are simultaneously digitized at 65 kHz using a Delta Sigma DAC (National Instruments, PCI 4474), and divided by the sum signal (using Labview) to obtain a signal independent of the intensity variations of the trap beam. The detector plane is conjugated with the back-focal plane of the objective. The photodiode is therefore only sensitive to the position of the bead with respect to the center of the trap. When a CCD camera is used in place of the QPD, we observe the interference pattern shown in Figure 1 above the QPD.

The sample used for calibration consists in a microfluidic chamber between a glass slide and a coverslip filled with 20 µL of a solution of 3 µm polystyrene beads (Polybead Carboxylate 3.00 ± 0.07 µm microspheres) diluted to 1:10^4 (v/v) in de-ionized water.

3 Bead position calibration

Measuring the lateral force on the bead requires a calibration of the position of the bead in x and y with respect to the center of the trap, as well as a calibration of the stiffness of the trap. Both of these can be inferred from the QPD signal, provided the conversion factor between the normalized QPD signal and the position in nm of the trapped bead is calibrated. In addition, the most common method for trap stiffness calibration, namely the power spectrum method, as well as the step response method, require a good knowledge of the bead height, since viscous drag rapidly increases close to the surface. This variation is known as Faxén's law [6].

3.1 Calibration of bead height – Interference pattern in reflection

We monitored the spatial distribution of the interference between the light reflected by the bead and that reflected by the coverslip, by placing a camera instead of a QPD in a plane conjugate with the back focal plane of the objective. The reflection on the top surface of the coverslip is due to the difference in refractive index between the liquid and the glass. Figure 2 shows the well contrasted rings that are observed for different heights of the bead with respect to the coverslip.

This pattern gives us information about the height of the bead. In the center of the pattern, i.e. for normal incidence on the bead, the optical path difference is:

$$\delta(d) = 2n_f d + \lambda/2, \tag{1}$$

where n_f is the refractive index of the liquid surrounding the bead and d the distance between the top surface of the coverslip and the bottom of the bead. When the distance between the bead and the surface is increased starting from a position of contact of the bead on the surface, the center of the interference pattern alternates between dark and bright fringes with a period $D = \lambda/2n_f = 402$ nm. This gives us directly the height of the bead center $h = d + R$ where R is the radius of the bead. Note that identifying the full interference pattern gives us directly the bead height without having to count the number of dark fringes from height zero.

As a confirmation of this model, we measured the distance d inferred from the center of the interference pattern as a function of the displacement of the piezo-stage in the z direction. We found a ratio $D_{\text{piezo}}/D = 1.24 \pm 0.05$ compatible with a ratio of 1.18 calculated from the refraction at the coverslip-liquid interface (respective refractive indices 1.52 and 1.33), with a small correction by spherical aberration further lowering the focusing plane of the trapping laser (see Appendix).

3.2 Calibration of the lateral position of the bead

The conversion factor between the normalized QPD signal S_0 and the position in nm of the trapped bead with respect to the center of the trap was determined in both
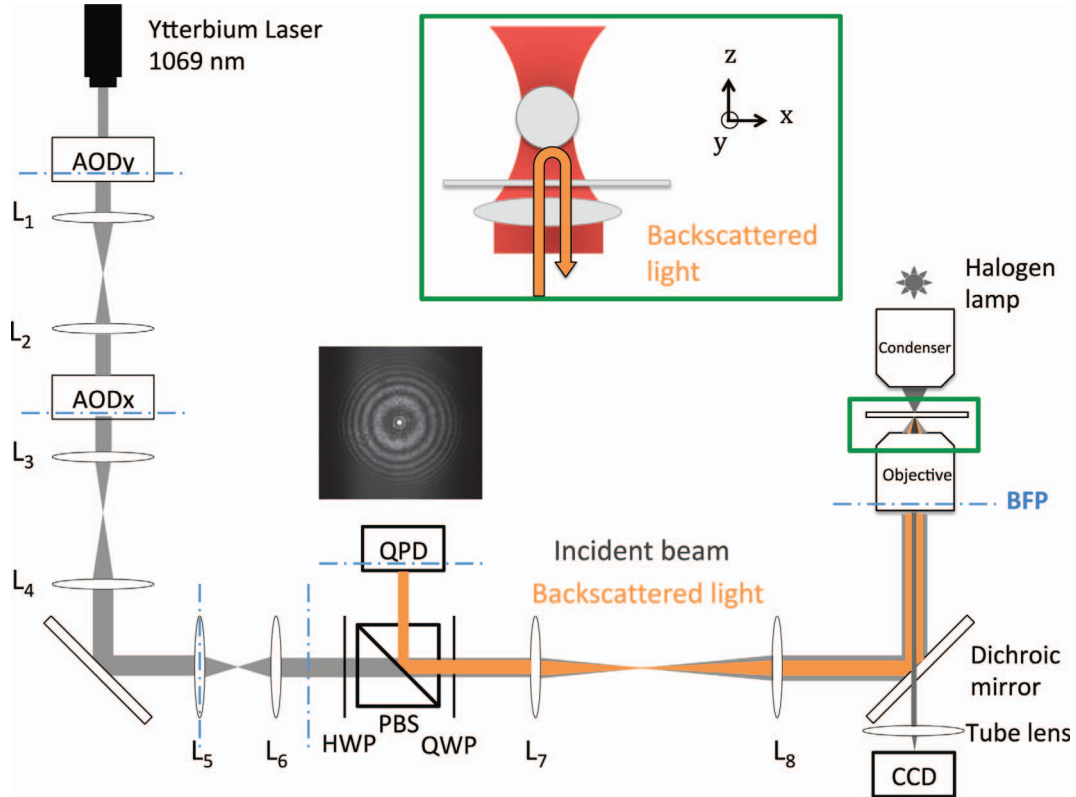
Figure 1. Experimental setup. Dashed lines on AOD_y, AOD_x, L_5, BFP and QPD represent conjugated planes. A half wave plate (HWP) maximizes transmission through the polarizing beamsplitter cube (PBS). The trap beam is reflected by a dichroic mirror (Chroma 725 DCSPXR) that also transmits the white light used to image the trapped bead on the CCD camera (U-Eye, UI 2240 SE MGL). A quarter wave plate (QWP) ensures that the backscattered light from the trapped bead, as shown in the insert, is reflected by the PBS and detected on either a QPD or a CCD camera. The interference pattern shown is observed when using the CCD camera. Focal lengths are: $f_1 = f_2 = f_3 = 150$ mm, $f_4 = 200$ mm, $f_5 = f_6 = 50$ mm, $f_7 = 300$ mm and $f_8 = 400$ mm.

directions x and y using the step-response method, as described in [11]. In this method, the trap beam is moved rapidly by a known distance, and we measure the QPD signal as the bead comes back into the trap. The initial signal gives the position calibration, and the decay time the stiffness. Figure 3 shows the calibration of the detector over displacements from -600 nm to 600 nm at a given height (2.7 µm) and laser power (230 mW) when using the objective without a phase ring. As expected, the response is linear for small displacements. A saturation appears when the bead moves further than 300 nm, a distance on the order of the laser waist at the focus (500 nm in our setup).

Figure 4 shows the QPD signal for a displacement x_0 of 300 nm as a function of the height of the bead center. With the objective without phase ring, we observed oscillations on the order of 5% for different heights of the bead (see red squares in Fig. 4). When the bead moves from the center of the trap, the center of the interference pattern observed in the objective back focal plane moves. Close to the surface, when there are only a few rings in the pupil (as in Fig. 2a), the vignetting by the pupil induces a small variation in the calibration signal depending on the interference order at the center. We thus calibrated the detector for each bead height.

3.3 Effect of a phase ring

For this section, we used the phase-contrast objective. We calibrated the QPD, as in Section 3.2. The results are plotted in Figure 4 (blue circles). In this case, the signal of the QPD depends strongly on the trapped bead height (almost 20% change for half an interference order on the interference pattern). This has not been reported when the QPD is placed in a plane conjugated with the condenser BFP [21]. This effect is due to the fact that the phase ring is located in the objective BFP, and is thus imaged onto the QPD (see Fig. 2d). Depending on the trapped-bead height, the phase ring blocks either a dark or a bright portion of the interference pattern, leading to large differences in the QPD sensitivity. To avoid this problem, it is necessary to deport the phase ring outside the microscope objective, in a plane conjugate to the pupil in the imaging path.

4 Trap stiffness calibration – comparison of the different methods

Using the above position calibrations, we have made a comparison of four different methods to determine the stiffness
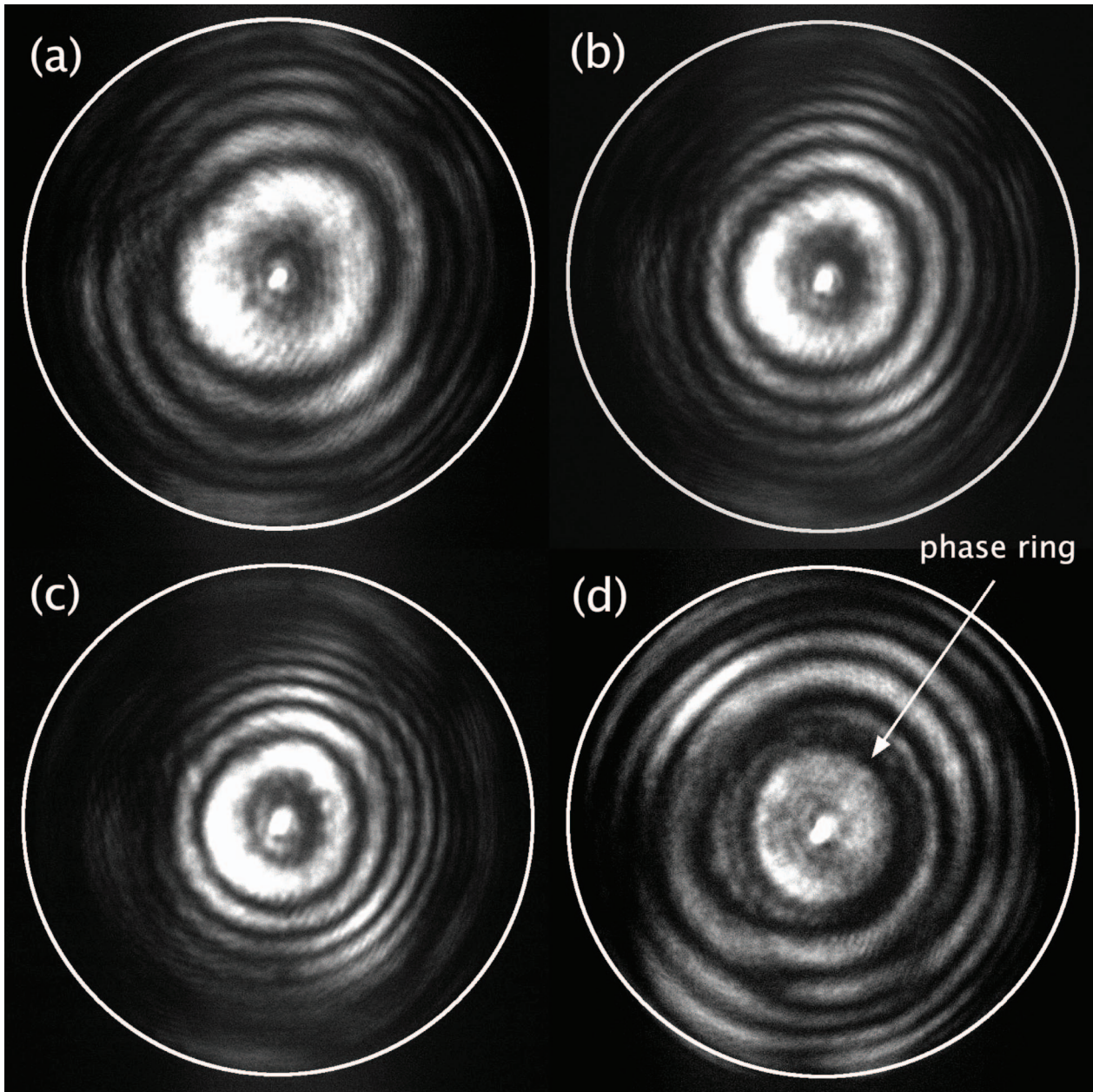
Figure 2. Interference patterns observed in the back-focal plane of the objective at different distances d between the top surface of the coverslip and the bottom of the bead: (a) $d = 5D$, (b) $d = 10D$, (c) $d = 15D$. D is the period between two dark fringes at the center of the interference pattern. Image (d) was obtained at $d = 5D$ with a phase contrast objective, showing the phase ring in its back focal plane. The white circles show the edge of the objective pupil, with a diameter of 5.2 mm.

of our optical tweezer. The methods fall into two categories. In the first two, step response and power spectrum analysis, a knowledge of the viscous drag is necessary to obtain a quantitative measurement. This point is critical because the drag is significantly modified when the bead is within a few microns of a surface such as a cover slip. By contrast, the other two methods, equipartition and Bayesian inference, do not require a knowledge of this drag, but they can be sensitive to other systematic effects, in particular the low frequency noise in the system. We have successfully corrected the systematic effects in three of these methods as we describe in the following.

4.1 Trap calibration methods

All measurements were performed using the objective without the phase ring. In order to compare the four different calibration methods, the Brownian motion and the step-response of the same trapped bead were recorded in both directions x and y. For each height and laser power,
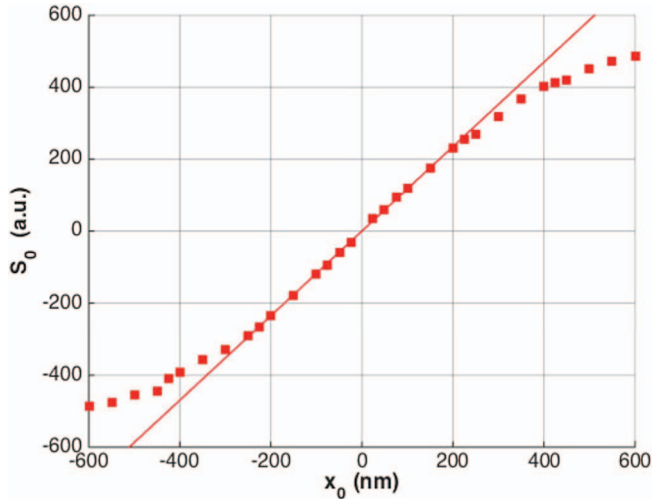
Figure 3. Calibration of the QPD in the xy plane. The linear fit gives the factor to convert raw data from the QPD into a distance in nm. Data was taken for a bead trapped at a height $h = 2.7$ μm above the coverslip surface with a laser power of 230 mW and an objective without phase ring. Error bars corresponding to the average over 10 data sets are within the width of the plotting symbols.
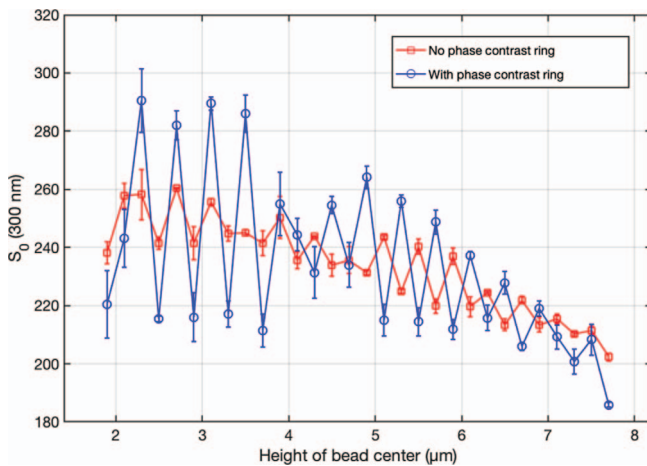

Figure 4. Signal of the QPD in the xy plane for a displacement of the bead of 300 nm, versus trapped-bead height. The height is calculated from the number N of dark fringes observed from contact to the slide as $h = ND + R$, with $D = 402$ nm and $R = 1.5$ μm. The values obtained using the objective with a phase contrast ring (blue) or without (red) are compared.

10 data sets of 30 steps of 100 nm were acquired with the same bead, and the QPD calibration was performed each time.

For the step-response method, the 30 steps in each data set were averaged and fitted to obtain a relaxation time. The trap stiffness is deduced from the average of those 10 fitted values, with error bars corresponding to their standard deviation. The relaxation time scales were all less than 400 μs.

For the power spectrum analysis, we took one Brownian motion trajectory of 8 s for each height. This data was processed using the program published in [22]. The Fourier Transform of the Brownian motion trajectory is fitted by

$$P(f) = \frac{D/2\pi^2}{f_c^2 + f^2}\left(\alpha^2 + \frac{1 - \alpha^2}{1 + (f/f_d)^2}\right), \qquad (2)$$

where D is the diffusion coefficient, f_c the trap cutoff frequency, f_d is the QPD cutoff frequency and α the fraction of charge carriers created in the depletion area. The two latter parameters are introduced to take into account the finite temporal response of the photodiode [23]. Because of the presence of low frequency noise (see Fig. 5), we restricted the range of the fit to frequencies above 200 Hz, except for the 2 lowest laser power values for which the restriction was above 100 Hz. The error bars on the stiffness determined by the power spectrum method shown in Figures 6 and 8 are those given by the fitting procedure. They are probably an underestimate of the uncertainty because of the presence of the low frequency noise. Note that, when fitting the data, we found a fraction α of a few percent, compatible with zero and f_d above 6 kHz. The same values were found from the step-response method.

For the Bayesian inference method, the same 8-second trajectory was divided into six sub-trajectories of 8000 data points, keeping only one every 10 points to eliminate the memory effect due to the limited temporal response of the QPD (given by the previous fit results giving f_d and α) compared to the data sampling rate [12]. The error bars are the result of the quadratic sum of the standard deviation between the data sets and the error on the QPD calibration coefficient.

For the equipartition method, the entire Brownian motion trajectory was considered and only the error on the QPD calibration coefficient was taken into account. From the measured power spectrum, using Parseval's theorem, we evaluated the low frequency noise contribution and corrected $\langle x^2 \rangle$ to keep only the relevant contribution as in ref. [24].

4.2 Results and discussion

Figure 6 compares the stiffness of the trap, obtained from the step-response method and the power spectrum analysis, at different heights h, for a fixed laser power (230 mW). These two methods rely on the knowledge of the viscous drag at the trapping height to calculate the trap stiffness, given by Faxén's law as a function of the height of the bead. This height was measured accurately, using the interference pattern as described in Section 3.1. As shown in Figure 6, the correction is substantial and leads to a trap stiffness independent of height. This indicates that no significant degradation of the stiffness due to spherical aberration is observed over this range of heights. Unlike what was reported in [25], this is in good agreement with theoretical predictions in [26] as well as our own calculation shown in Appendix, giving a decrease of only a few percent for lateral trap stiffness over the first 10 μm.
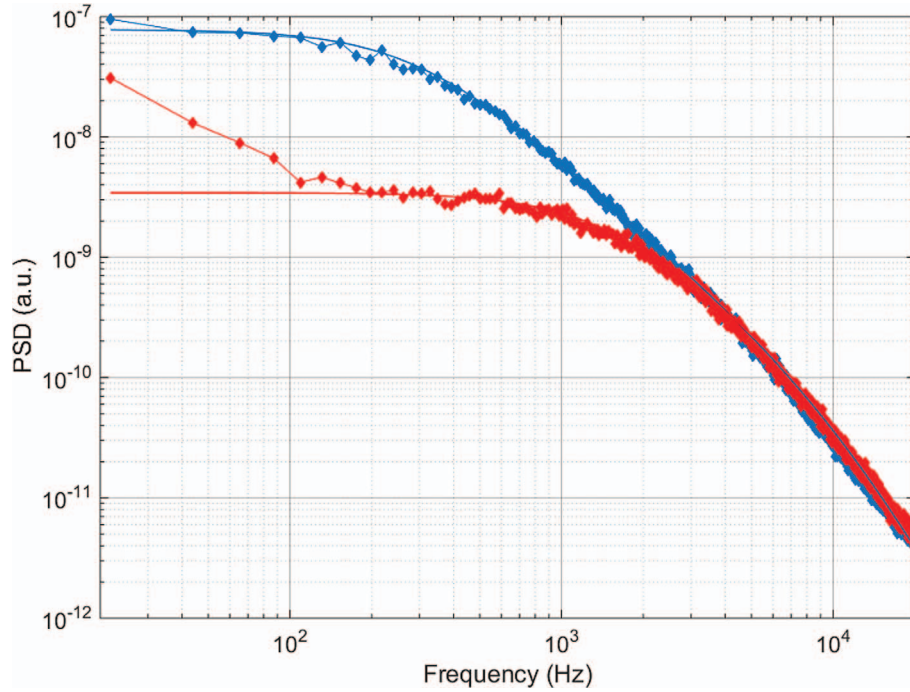
Figure 5. Power spectrum density as a function of frequency for laser powers of 140 mW (blue markers) and 650 mW (red markers). The solid lines are corresponding fits for frequencies above 100 Hz (blue) and above 200 Hz (red). Low frequency noise appears on the red curve as the first ten points below 200 Hz.
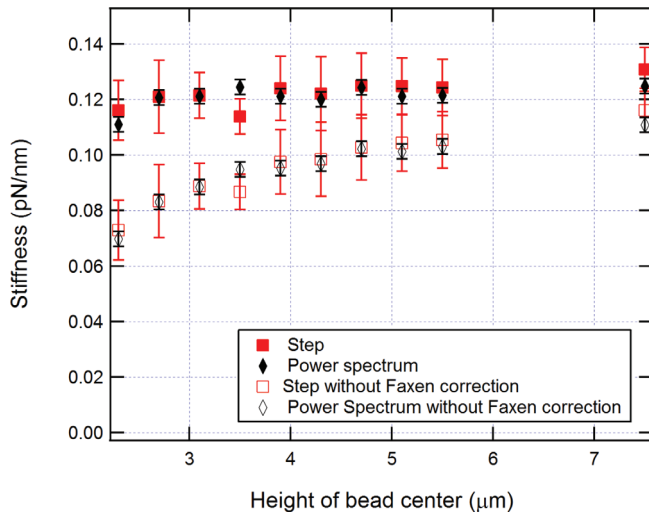

Figure 6. Stiffness of the trap obtained with the step-response and the power spectrum analysis for different heights of the trapped bead, with or without taking into account Faxén's correction for the viscous drag near the surface. Laser power at the entrance of the objective was fixed at 230 mW.

Figure 7. Stiffness of the trap obtained with the Bayesian inference and the equipartition methods, for different heights of the trapped bead. Laser power at the entrance of the objective was fixed at 230 mW.

Figure 7 compares the stiffness of the trap, obtained from the Bayesian inference and equipartition methods under the same conditions. They confirm that the stiffness does not depend on bead height. Once corrected for low frequency noise, the stiffness obtained by the equipartition method agr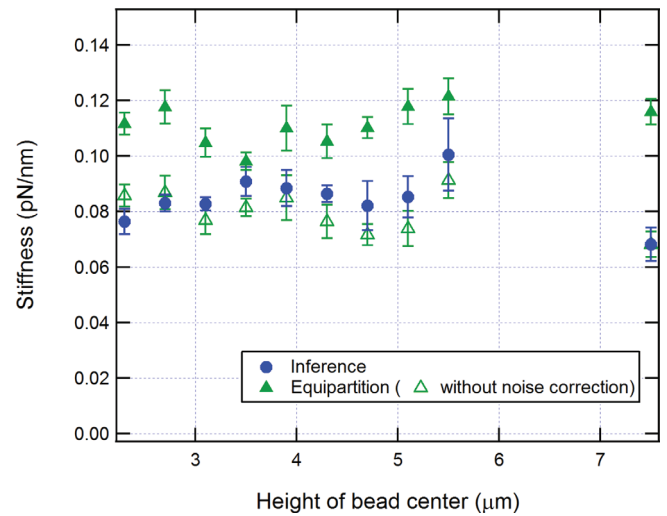ees to better than 10% with the previous two methods. Since the Bayesian inference approach can in principle exploit the full information of the motion from one space-time point to the next, shorter trajectories might have been used to reduce the effect of this low frequency noise, as shown in [12]. This was not possible here due to the absence of an instantaneous fraction in the response of our detector (α; 0, compared to $\alpha = 0.3$ in [12]).
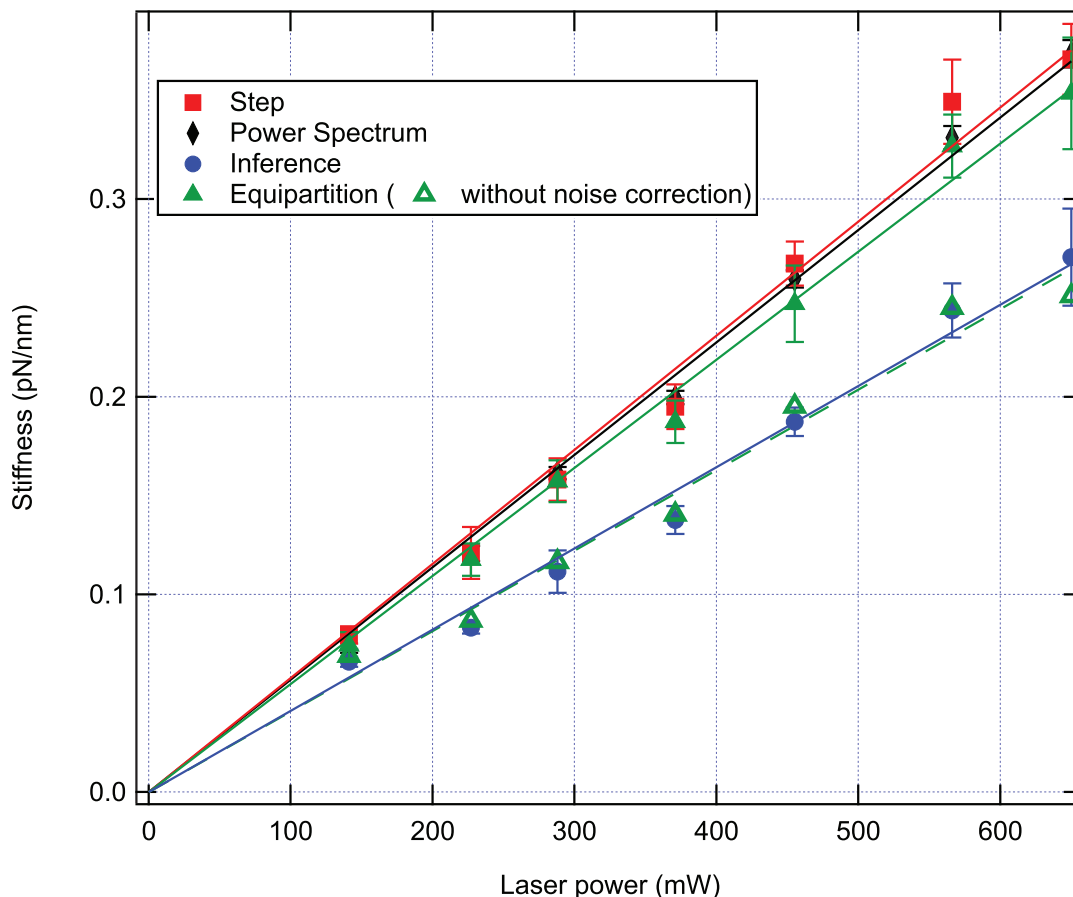
Figure 8. Trap stiffness, obtained with the four calibration methods, as a function of the incident laser power, measured at the entrance of the objective. The height is fixed at 2.7 μm. For each calibration method, a linear fit is superimposed.

Figure 8 shows the dependence of the stiffness with laser power, for a fixed height (2.7 μm). We see the expected linear behavior of the trap stiffness with laser power for all four methods. The stiffness values obtained by the step-response, power spectrum analysis and equipartition theorem are in very good agreement, while the Bayesian inference method gives values that are lower by 25%. Correcting for the presence of the low frequency noise in the Bayesian inference method would require including the diode response function in the inference algorithm. The observed linearity confirms that the corrections we have made to the various measurements are independent of laser power.

5 Conclusion

In this article, we have shown that an accurate calibration of optical tweezers can be achieved using backscattered light. The well contrasted interference pattern observed in the back focal plane of the microscope objective, due to the reflections on the coverslip and on the bead, is an asset to precisely determine the trapped bead height. The information about the bead height allows us to correctly account for the behaviour of the viscous drag close to a surface.

Remarkably, this interference pattern does not affect the linearity of the lateral position calibration over a range of 250 nm away from the center of the trap. Four calibration methods, step-response, power spectrum density, equipartition and Bayesian inference were implemented in this configuration, and compared as a function of height and laser power. We were able to carry out this calibration between 2.5 and 7.5 μm from the surface and up to 600 mW of laser power reaching a stiffness of 0.35 pN/nm. Results are for the most part in very good agreement and are independent of bead height, showing no reduction of stiffness due to spherical aberrations in this range of heights. The remaining discrepancy is well understood, and the choice of calibration method depends on environmental factors such as acoustic noise or detector's properties.

This method makes the optical tweezer a self-contained module where application of the force and in situ monitoring of its value can be added to an existing setup without interfering with other modalities. We have also demonstrated the combination of backscattered calibration with phase contrast microscopy, provided that the phase ring is deported in the imaging path. Fluorescence microscopy is another modality that can be combined with this versatile optical tweezer setup on live cells, as a key to the understanding of mechanotransduction, i.e. how cells sense

physical forces and how they are translated into biochemical and biological responses. As an example, such a setup can correlate external force application by optical tweezers to FRET based force measurements on internal proteins under tension such as vinculin or talin at focal adhesion sites.

Over the height range explored in this article, spherical aberration is responsible for a slightly larger focal shift (by 1.18 instead of the index ratio 1.14), a small decrease of the maximal intensity of the focused beam (less than 10%) and a 10% increase of the full width at half maximum. We conclude that spherical aberration has no significant impact on the trapping beam in this range.

References

1 Bustamante C.J., Chemla Y.R., Liu S., Wang M.D. (2021) Optical tweezers in single-molecule biophysics, *Nat. Rev. Methods Primers* **1**, 25.

2 Arbore C., Perego L., Sergides M., Capitanio M. (2019) Probing force in living cells with optical tweezers: from single-molecule mechanics to cell mechanotransduction, *Biophys. Rev.* **11**, 765–782.

3 Favre-Bulle I.A., Scott E.K. (2022) Optical tweezers across scales in cell biology, *Trends Cell Biol.* **32**, 932–946.

4 Gieseler J., Gomez-Solano J.R., Magazzù A., Perez-Castillo I., Perez-Garcia L., Gironella-Torrent M., Viader-Godoy X., Ritort F., Pesce G., Arzola A.V., Volke-Sepùlveda K., Volpe G. (2021) Optical tweezers – from calibration to applications: a tutorial, *Adv. Optics Photon.* **13**, 74.

5 Berg-Sørensen K., Flyvbjerg H. (2004) Power spectrum analysis for optical tweezers, *Rev. Sci. Instrum.* **75**, 3, 594–612.

6 Neuman K.C., Block S.M. (2004) Optical trapping, *Rev. Sci. Instrum.* **75**, 9, 2787–2809.

7 Thalhammer G., Obmascher L., Ritsch-Marte M. (2015) Direct measurement of axial optical forces, *Optics Exp.* **23**, 6112.

8 Bui A.A.M., Kashchuk A.V., Balanant M.A., Nieminen T. A., Rubinsztein-Dunlop H., Stilgoe A.B. (2018) Calibration of force detection for arbitrarily shaped particles in optical tweezers, *Sci. Rep.* **8**, 10798.

9 Visscher K., Gross S.P., Block S.M. (1996) Construction of multiple-beam optical traps with nanometer-resolution position sensing, *IEEE J. Quantum Electron.* **2**, 1066–1076.

10 Singer W., Bernet S., Hecker N., Ritsch-Marte M. (2000) Three-dimensional force calibration of optical tweezers, *J. Mod. Opt.* **47**, 2921–2931.

11 Le Gall A., Perronet K., Dulin D., Villing A., Bouyer P., Visscher K., Westbrook N. (2010) Simultaneous calibration of optical tweezers spring constant and position detector response, *Optics Exp.* **18**25, 26469–26474.

12 Richly M.U., Türkcan S., Le Gall A., Fiszman N., Masson J.-B., Westbrook N., Perronet K., Alexandrou A. (2013) Calibrating optical tweezers with Bayesian inference, *Optics Exp.* **21**, 25, 31578–31590.

13 Argun A., Thalheim T., Bo S., Cichos F., Volpe G. (2020) Enhanced force-field calibration via machine learning, *Appl. Phys. Rev.* **7**, 041404.

14 Gittes F., Schmidt C.F. (1998) Interference model for back-focal-plane displacement detection in optical tweezers, *Opt. Lett.* **23**, 7–9.

15 Shipley F.B., Carter A.R. (2012) Back-scattered detection yields viable signals in many conditions, *Optics Exp.* **20**, 9581.

16 Keyser U.F., van der Does J., Dekker C., Dekker N.H. (2006) Optical tweezers for force measurements on DNA in nanopores, *Rev. Sci. Instrum.* **77**, 105105.

17 Sischka A., Kleimann C., Hachmann W., Schäfer M.M., Seuffert I., Tönsing K., Anselmetti D. (2008) Single beam optical tweezers setup with backscattered light detection for three-dimensional measurements on DNA and nanopores, *Rev. Sci. Instrum.* **79**, 063702.

18 Huang L., Guo H., Li K., Chen Y., Feng B., Li Z.-Y. (2013) Three dimensional force detection of gold nanoparticles using backscattered light detection, *J. Appl. Phys.* **113**, 113103.

19 Samadi A., Masoumeh Mousavi S., Hajizadeh F., Reihani S. N.S. (2019) Backscattering-based detection scheme for dark-field optical tweezers, *J. Opt. Soc. Am. B* **36**, 1587.

20 Neuman K.C., Abbondanzieri E.A., Block S.M. (2005) Measurement of the effective focal shift in an optical trap, *Opt. Lett.* **30**, 1318.

21 Mahmoudi A., Reihani S.N.S. (2010) Phase contrast optical tweezers, *Optics Exp.* **18**, 17, 17983–17996.

22 Hansen P.M., Tolic-Nørrelykke I.M., Flyvbjerg H., Berg-Sørensen K. (2006) tweezercalib 2.0: Faster version of MatLab package for precise calibration of optical tweezers, *Comput. Phys. Commun.* **174**6, 518–520.

23 Berg-Sørensen K., Oddershede L., Florin E.-L., Flyvbjerg H. (2003) Unintended filtering in a typical photodiode detection system for optical tweezers, *J. Appl. Phys.* **93**, 6, 3167–3176.

24 Perkins T.T. (2009) Optical traps for single molecule biophysics: a primer, *Laser Photon. Rev.* **3**, 1–2, 203–220.

25 Vermeulen K.C., Wuite G.J.L., Stienen G.J.M., Schmidt C. F. (2006) Optical trap stiffness in the presence and absence of spherical aberrations, *Appl. Opt.* **45**, 1812.

26 Rohrbach A., Stelzer E.H.K. (2002) Trapping forces, force constants, and potential depths for dielectric spheres in the presence pf spherical aberrations, *Appl. Opt.* **41**, 13, 2494–2507.

27 Hugonin J.P., Besbes M., Lalanne P. (2008) Hybridization of electromagnetic numerical methods through the G-matrix algorithm, *Opt. Lett.* **33**, 14, 1590–1592.

Appendix

A.1 Effect of spherical aberration on the trapping beam

Using the hybridized electromagnetic numerical method published in [27], we calculated the intensity of the trapping laser focused beam after refraction at the coverslip-water interface and compared it with the intensity of a focused beam with no index mismatch on its path. The results are presented in Figure A1.
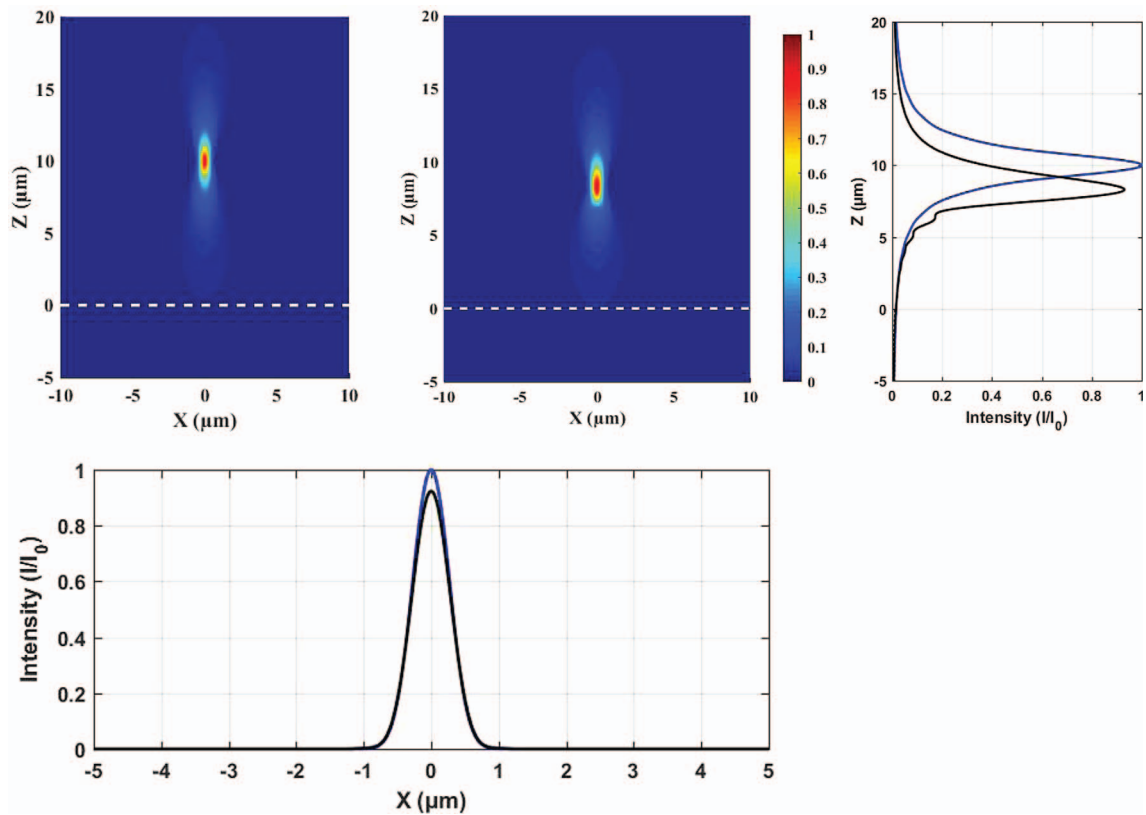
Figure A1. Normalized intensities of highly focused beams that propagate along the z direction with no index mismatch (left) or with $n = 1.52$ for $z < 0$ and $n = 1.33$ for $z > 0$ (right). We compare a focus 10 μm above the coverslip with no index mismatch with the actual focus taking spherical aberration into account with the index mismatch. The focus is closer to the interface by a factor of 1.18. The interface location is shown by the dashed white line. Far right, and bottom: line scan through the points of maximal intensities (blue: focus with no index mismatch; black: with mismatch).